Chinese Chemical Letters 35 (2024) 109429

Contents lists available at ScienceDirect

Chinese Chemical Letters

journal homepage: www.elsevier.com/locate/cclet

A self-cleaning window for high-efficiency photodegradation of indoor formaldehyde

Changzhu Huang[a,b], Wei Dai[b], Shimao Deng[b,c], Yixin Tian[a,b], Xiaolin Liu[a,*], Jia Lin[a,*], Hong Chen[b,*]

[a] *Department of Physics, Shanghai Key Laboratory of Materials Protection and Advanced Materials in Electric Power, Shanghai University of Electric Power, Shanghai 200090, China*
[b] *Shenzhen Key Laboratory of Interfacial Science and Engineering of Materials, State Environmental Protection Key Laboratory of Integrated Surface Water-Groundwater Pollution Control, Guangdong Provincial Key Laboratory of Soil and Groundwater Pollution Control, School of Environmental Science and Engineering, Southern University of Science and Technology, Shenzhen 518055, China*
[c] *Eastern Institute for Advanced Study, Eastern Institute of Technology, Ningbo 315200, China*

ARTICLE INFO

Article history:
Received 27 September 2023
Revised 22 November 2023
Accepted 13 December 2023
Available online 24 December 2023

Keywords:
Bismuth tungstate
Resorcinol-formaldehyde
Photocatalysis
Hydrogen peroxide
HCHO degradation

ABSTRACT

Formaldehyde (HCHO) as an indoor air pollutant released by new furniture and decorative materials is of great concern. Developing a self-cleaning device to remove HCHO is an ideal way to improve indoor air quality. In this study, a self-cleaning window with a multilayered structure constructed from fluorine-doped tin oxide/bismuth tungstate/resorcinol-formaldehyde resin (FTO/Bi_2WO_6/RF) has been fabricated, which is capable of degrading HCHO in natural indoor condition. The as-fabricated device could utilize the natural room light and promote the generation and transfer of the photocatalytic carriers in Bi_2WO_6, which subsequently delivers a good catalytic oxygen reduction efficiency in RF to produce hydrogen peroxide (H_2O_2). The as-synthesized H_2O_2 could further split into hydroxyl radicals (${}^{\bullet}OH$), then oxide the HCHO molecules in the air. The present study demonstrates a novel and efficient strategy to fabricate a transparent multifunctional window for self-cleaning indoor gaseous pollutants, the concept is of great importance to be expanded in a broad range of indoor furniture for in-house air pollution control.

© 2024 Published by Elsevier B.V. on behalf of Chinese Chemical Society and Institute of Materia Medica, Chinese Academy of Medical Sciences.

Indoor volatile toxic gases (VOCs) emitted from interior building decoration materials, such as wooden furniture, wallpaper, and paint, are the primary sources of indoor air pollution [1,2]. As one of the most representative and direct indoor VOCs, formaldehyde (HCHO) poses a significant risk to human nerve and respiratory systems [3,4]. In 2006, HCHO was classified as a major indoor air pollutant and Group I carcinogen compound by the International Agency for Research on Cancer (IARC) [5]. Furthermore, HCHO is a challenge in terms of quickly degrading and can affect indoor air quality for up to six months [6,7]. Therefore, effectively removing indoor HCHO is imperative to improve indoor air quality and protect human health [8]. Among various methods reported for HCHO purification [9–11], adsorption is widely used owing to its easy operation and low cost. However, the adsorbed HCHO may re-release from the adsorbent to the environment, resulting in a secondary cycle of pollution [12,13]. Thermal catalysis can mineralize HCHO into non-toxic products such as CO_2 and H_2O; however, high energy consumption is required, restricting its application for indoor air purification under natural conditions [14–16]. Therefore, it is necessary to develop green and sustainable technologies to effectively degrade the indoor HCHO and control the air quality.

Photocatalytic technologies are attracting increasing attention because they convert solar energy into environmentally friendly energy carriers for pollutant degradation. Various photocatalysts have been developed to ensure cost-effective and highly efficient photocatalytic processes [12,13,17]. Although a variety of photocatalysts have been explored for HCHO degradation, most of the photocatalysts explored nowadays are powders. During the practical application in indoor room air control, these photocatalyst powders are difficult to apply and can be easily inhaled into the human body, resulting in subsequently adverse human health impact [18].

In this study, we first coated multiple layers of bismuth tungstate (Bi_2WO_6) and resorcinol-formaldehyde resin (RF) films onto the fluorine-doped tin oxide (FTO) substrate *via* continuous hydrothermal reactions to construct a photocatalytic window with a distinct sandwich structure. The multiple-layered FTO/Bi_2WO_6/RF thin films demonstrated high photocatalytic efficiency and strong

---

* Corresponding authors.
E-mail addresses: xlliu@shiep.edu.cn (X. Liu), jlin@shiep.edu.cn (J. Lin), chenh3@sustech.edu.cn (H. Chen).

https://doi.org/10.1016/j.cclet.2023.109429
1001-8417/© 2024 Published by Elsevier B.V. on behalf of Chinese Chemical Society and Institute of Materia Medica, Chinese Academy of Medical Sciences.

oxidation capacity toward the effective removal of indoor HCHO gas. This work provides a new concept for designing multilayer self-cleaning windows for indoor air quality control, which paves the way for the construction of smart furniture for a sustainable environment.

To construct the self-clean window, Bi_2WO_6 has been coated on FTO to construct the FTO/Bi_2WO_6 *via* a hydrothermal method. Briefly, 0.97 g of $Bi(NO_3)_3 \cdot 5H_2O$, 0.32 g of $Na_2WO_4 \cdot 2H_2O$, and 0.01 g of cetyltrimethylammonium bromide (CTAB) were added in 16 mL of ethylene glycol and stirred for 1 h. The mixture was transferred into a 20 mL Teflon-lined stainless autoclave. Then, an FTO substrate was fully immersed in the solution in the autoclave with the conductive surface facing upwards with a tilted angle of 45°. The autoclave was heated in a 180 °C oven for 16 h to enable in-situ growth of Bi_2WO_6 on the FTO surface. After the reaction, the high-pressure autoclave was cooled down to room temperature naturally. The obtained FTO/Bi_2WO_6 was washed continuously with deionized (DI) water and anhydrous ethanol under sonication and dried in an oven at 60 °C to obtain a white Bi_2WO_6 film on the FTO surface. To further fabricate FTO/Bi_2WO_6/RF, 0.096 g of resorcinol powder was dissolved in a mixed solution containing formaldehyde (0.135 mL), ammonia (0.050 mL), and DI water (16 mL). After stirring for 30 min, the mixture was transferred into a 20 mL Teflon-lined stainless autoclave. The previously synthesized FTO/Bi_2WO_6 was fully immersed in the mixture, and the temperature of the convection drying oven was adjusted to 250 °C and heated for 24 h. Afterward, the resulting FTO/Bi_2WO_6/RF was cooled down and loaded in a beaker containing acetone solution, and sonicated for 1 min. Later, it was washed repeatedly with DI water and anhydrous ethanol, and dried in a vacuum drying oven at 80 °C for 10 h to obtain a reddish film. The detailed details have been shown in Fig. S1 (Supporting information), and documented in the Supporting information.

Photocatalytic experiments were conducted in a 60 mL homemade glass box using a Xenon lamp as a simulated light source. The full-spectrum light source was adjusted to one sun intensity by a light intensity meter, while the visible light source was obtained by filtering the UV light from the full spectrum using a 420 nm filter. 50 mL of DI water was added to a homemade box to simulate the indoor room environment. The FTO/Bi_2WO_6/RF film was placed vertically on the wall of the box. The surface containing the Bi_2WO_6/RF was aligned in the direction of the light source. 0.5 mL of the solution was extracted from the box into a 10 mL test tube every 1 h. Then 4.5 mL of cerium sulfate solution (0.05 mol/L) was added to this test tube and shaken to make sure a homogeneous solution was obtained. The absorbance of the solution was measured in the cuvette using a ultraviolet–visible (UV–vis) spectrophotometer, while the concentration of H_2O_2 produced by photocatalysis was calculated using the following equation (Eq. 1):

$$C_{H_2O_2} = \frac{V_0 \times C_0 - (V_0 + V_1)\ \times C_1}{2\ \times V_1} \tag{1}$$

where V_0 and C_0 are the volume and concentration of the prepared cerium ion solution; V_1 is the volume of the test solution; C_1 is the residue cerium concentration calculated from the absorbance and standard curves.

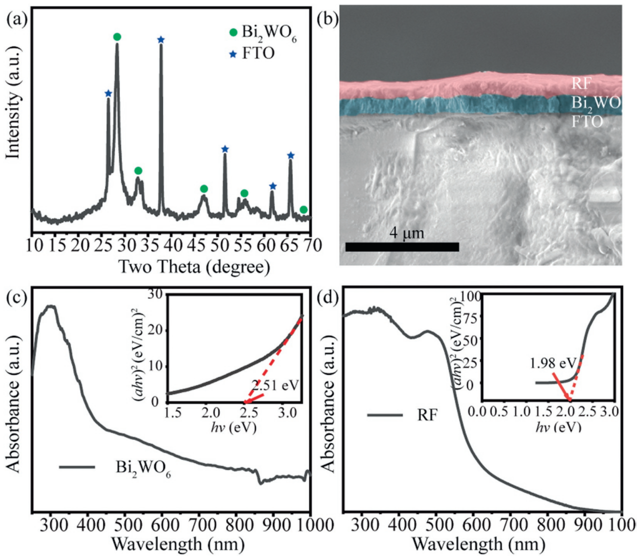

Fig. 1. (a) XRD pattern of FTO/Bi_2WO_6/RF. (b) Cross-sectional SEM image. (c) UV–vis diffuse reflectance spectra of Bi_2WO_6 and (d) RF resin. Inset: corresponding bandgaps estimated by plotting $(\alpha h\nu)^2$ *versus* $h\nu$, where α and ν are the absorbance and wavenumber, h is the Planck constant.

Powder X-ray diffraction (PXRD) was used to study the phase compositions of the as-synthesized different films (Fig. S2a in Supporting information). The XRD pattern of FTO/Bi_2WO_6/RF in Fig. 1a suggests that orthorhombic Bi_2WO_6 (space group B2ab (41), JCPDS 73–2020) [19] has been successfully growth on FTO, indicating a high purity of the as-prepared Bi_2WO_6 film [19]. Furthermore, a broad characteristic peak at approximately 20° corresponding to the amorphous RF resin has been observed, suggesting the RF resin has been successfully deposited on the film (Fig. S2b in Supporting information). To further study the morphology and elucidate the elemental distribution on FTO/Bi_2WO_6/RF, SEM and EDS mapping has been recorded as shown in Figs. S3a-f (Supporting information). It can be seen that the up surface of FTO/Bi_2WO_6/RF is covered by spherical RF resin, while all the elements are uniformly distributed within the film. To unravel the layered stacking structure of FTO/Bi_2WO_6/RF, a cross-sectional SEM image (Fig. 1b) has been recorded, which reveals that a sandwich structure has been preserved within FTO/Bi_2WO_6/RF film. The light-absorbing ability of a photocatalyst is critical to its photocatalytic activity, to study the optical properties of the as-prepared films. Solid-state UV–vis spectra have been recorded as shown in Fig. 1c. It can be seen that the absorption edge of the Bi_2WO_6 film was 480 nm. A steep absorption edge is observed in the visible range, indicating that Bi_2WO_6 presents a bandgap of 2.51 eV within the visible light area [20]. Moreover, an absorption edge of 650 nm corresponding to a bandgap energy of 1.98 eV has been also observed in Fig. 1d, this can be assigned to the charge transfer of the benzenoid units to quinoid units [21].

Furthermore, the surface elemental species and valence states of FTO/Bi_2WO_6/RF were analyzed using XPS. The change in binding energy was investigated which could be inferred from the tendency of electron transfer in FTO/Bi_2WO_6/RF [22–24]. As shown in Fig. S4 (Supporting information), the characteristic peaks associated with C, O, W, and Bi can be found in the full spectrum, demonstrating the presence of all the destinated elements in FTO/Bi_2WO_6/RF. Fig. 2a shows the XPS spectra of C 1s, the binding energies at 284.7, 286.5 and 287.6 eV are attributed to the chemical bonds of the sp^2 or sp^3 hybridized carbon within typical C=C, C–O, and C=O groups in RF, respectively [25,26]. Fig. 2b presents the high-resolution XPS spectrum of O 1s, wherein three characteristic peaks at binding energies of 529.9, 531.4 and 533.9 eV corresponding to the Bi-O, W-O, and O–H bonds are observed, respectively [25]. Furthermore, the W 4f peaks at 33.1 and 37.1 eV and Bi 4f peak at 164.3 and 159.0 eV, corresponding to the binding energies of W $4f_{7/2}$ and W $4f_{5/2}$, [27] and Bi $4f_{5/2}$ and Bi $4f_{7/2}$ [28] in Bi_2WO_6, have been observed in Figs. 2c and d, respectively. For comparison, the XPS spectra of FTO/Bi_2WO_6/RF under visible-light irradiation have also been recorded. Significant changes in peak positions of C 1s, O 1s, W 4f, and Bi 4f have been observed, indicating variations in the electron densities after light irradiation.

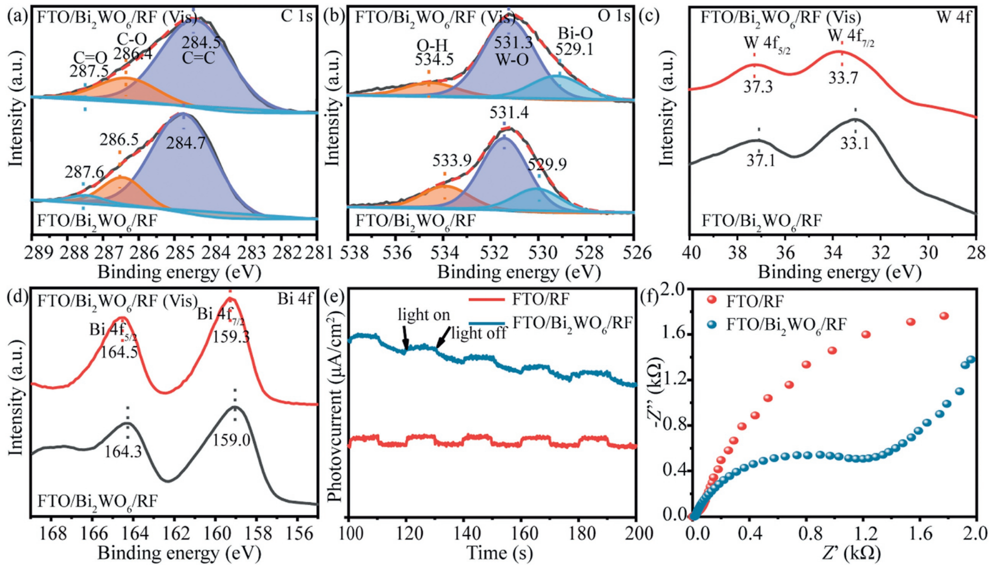

Fig. 2. XPS spectra of FTO/Bi_2WO_6/RF at (a) C 1s, (b) O 1s, (c) W 4f, and (d) Bi 4f core levels (Vis — the materials after light irradiation and another set without light exposure). (e) Transient photocurrent responses and (f) EIS plots of FTO/RF and FTO/Bi_2WO_6/RF.

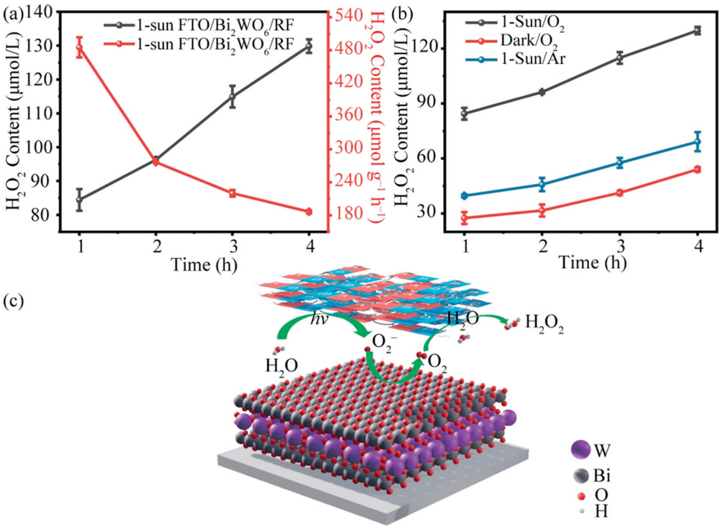

Fig. 3. Photocatalytic H_2O_2 generation of FTO/Bi_2WO_6/RF. (a) H_2O_2 concentration produced under 1 sunlight illumination and 4 h of continuous oxygen supply (black), H_2O_2 production rate over 4 h (red). (b) Effects of oxygen and light on the H_2O_2 production (black: with light and oxygen, blue: with light and without oxygen, red: with oxygen and without light). (c) Schematic diagram of oxygen cycles on Bi_2WO_6 and RF.

It is clear that under visible-light irradiation, the peak position of all the elements shows a redshift, which indicates a feasible electron transfer under light irradiation [24,29].

In addition, the transient photocurrent of FTO/RF, FTO/Bi_2WO_6, and FTO/Bi_2WO_6/RF are shown in Fig. 2e. The photocurrent response increases significantly from 0.05 μA to 0.11 μA in FTO/Bi_2WO_6/RF, which is ascribed to the synergetic effects of coupling Bi_2WO_6/RF together. Furthermore, the electrochemical impedance spectroscopy (EIS) spectra have been recorded in Fig. 2f, and a smaller radius has been observed within FTO/Bi_2WO_6/RF, compared with FTO/RF and FTO/Bi_2WO_6, suggesting a significantly reduced charge transfer resistance and benefited to the separation and transfer of photogenerated carriers [30,31].

The photocatalytic activity of the FTO/Bi_2WO_6/RF film for H_2O_2 production was investigated under 1 sun (100 mW/cm^2) irradiation with a simulated light source [32]. Fig. 3a shows a time-dependent H_2O_2 generation efficiency of FTO/Bi_2WO_6/RF film. The H_2O_2 generation concentrations are high at an early stage and continue to increase after prolonged light exposure. The overall H_2O_2 concentration reaches up to 130 μmol/L after 4 h, which is superior to the H_2O_2 concentrations generated by the photocatalyst powders as reported in the literature. Furthermore, the highest production rate of 480 μmol g^{-1} h^{-1} can be achieved at the early stage, while it decreases afterward (Table 1) [33–39]. The intrinsic reason could be ascribed to the fact that the as-generated holes (h^+) in the valence band (VB) of RF are accumulated as the reaction goes on, which is not only subjected to consumption by water oxidation but also by RF autoxidation [21].

To understand the H_2O_2 production mechanism, the influence of light and oxygen on photocatalytic H_2O_2 generation efficiency was studied (Fig. 3b). The red line indicates the produced H_2O_2 concentration after continuous passage of oxygen in the dark condition, while the black and blue lines represent the generated H_2O_2 concentrations under oxygen and argon environments under 1 sun irradiation. The results demonstrate that under anaerobic conditions, a 70 μmol/L H_2O_2 concentration in 4 h has achieved in

Table 1
Comparing the production of H_2O_2 among different photocatalysts.

Photocatalysts	Illumination wavelengths (nm)	Sacrificial agents	Light source	Evolution rates (μmol g^{-1} h^{-1})	Ref.
g-C_3N_4	$\lambda \geq 420$ nm	Ethanol	300 W Xenon Lamp	125	[33]
RF-NH_3–523	$\lambda \geq 420$ nm	Deionized water	250 W Xenon Lamp	215	[21]
g-C_3N_4/PDI/rGO	$\lambda \geq 420$ nm	Deionized water	300 W Xenon Lamp	11.2	[34]
$CoWO_4$@Bi_2WO_6	$\lambda \geq 420$ nm	Deionized water	300 W Xenon Lamp	50	[35]
PF_2FBT/TiO_2	$\lambda \geq 420$ nm	Deionized water	300 W Xenon Lamp	55.2	[36]
Bi/BiOBr-CdS	$\lambda \geq 420$ nm	Deionized water	300 W Xenon Lamp	346.6	[37]
CdS/RGO/Fe^{2+}	$\lambda \geq 420$ nm	Deionized water	300 W Xenon Lamp	290.34	[38]
N Vacancy g-C_3N_4	$\lambda \geq 400$ nm	Ethanol+deionized water	300 W Xenon Lamp	288.9	[39]
FTO/Bi_2WO_6/RF	$\lambda \geq 420$ nm	Deionized water	300 W Xenon Lamp	480	This work

FTO/Bi_2WO_6/RF, which should be account to the fact that photocatalytic O_2 production capability of Bi_2WO_6 combined with the oxygen reduction ability of RF, which helps to split the water molecule to generate O_2, then further reduced to produce H_2O_2 [40], as it is well-known that Bi_2WO_6 is a capable of photocatalytic water oxidation to highly efficient generating O_2 [41,42]. Moreover, the concentration of H_2O_2 produced by FTO/Bi_2WO_6/RF and FTO/RF under anaerobic conditions are compared and shown in Fig. S5 in Supporting information. It is clear that under the presence of Bi_2WO_6, the generated H_2O_2 concentration is 3–4 times higher than solely with RF, indicating that the oxygen produced by Bi_2WO_6 *via* photocatalytic water splitting pathway plays a critical role in the efficient production of H_2O_2 in the FTO/Bi_2WO_6/RF system. It may serve as the oxygen source for photocatalytic reduction to produce H_2O_2. As shown in Fig. 3c, it illustrates the process of bismuth tungstate generating oxygen and the resin reducing oxygen. Water molecules adsorb onto the bottom layer of the Bi_2WO_6 film, where the oxygen atom of the water molecule donates an electron, forming oxygen ions (O_2^-). The generated O_2^- are released onto the catalyst surface, where they combine with holes to produce O_2. O_2 is then transported to the upper layer RF, where it participates in the oxygen reduction reaction with the electrons escaping from its surface, accelerating the production of H_2O_2. The specific formula is as follows (Eq. 2) [43,44]:

$$O_2 + 2e^- + 2H^+ \rightarrow H_2O_2 \tag{2}$$

As shown in Fig. 4a, the production of H_2O_2 increased with the light intensity. The stronger the light intensity, the more H_2O_2 is produced. Fig. 4b compares the H_2O_2 concentrations produced by different films under the same light intensity. FTO/Bi_2WO_6/RF generates more H_2O_2 than FTO/RF and FTO/Bi_2WO_6. In addition, the H_2O_2 production ability of FTO/Bi_2WO_6/RF under different light intensities (0.5 and 1 sun) was investigated.

To understand the energy diagram and electron transfer pathway, the energy structure of the material consisted within the film has been carefully characterized (Fig. 4c). Mott-Schottky measurements were conducted to calculate the conduction band (CB) and valence band (VB) positions of Bi_2WO_6 and RF. As shown in Fig. S6 (Supporting information), both Bi_2WO_6 and RF are n-type semiconductors with positive slopes and their flat-band potentials are −0.87 and −0.48 V, respectively. The CB positions *versus* the standard hydrogen electrode (SHE) were converted using the following equation (Eq. 3) [45,46]:

$$E\ (vs.\ \mathrm{RHE}) = E\ (vs.\ \mathrm{SCE}) + 0.0591\mathrm{pH} + 0.2 \tag{3}$$

The calculated CB positions of Bi_2WO_6 and RF are −0.22 and 0.173 V, respectively [47]. Therefore, based on the respective band gaps of 2.51 and 1.98 eV for Bi_2WO_6 and RF, the valence band positions can be determined as 2.290 and 2.153 eV, respectively. By analyzing the energy band structure and conducting photoelectrochemical tests on the FTO/Bi_2WO_6/RF film, its high photocatalytic activity may be attributed to the efficient transfer of photo-induced electrons [48].

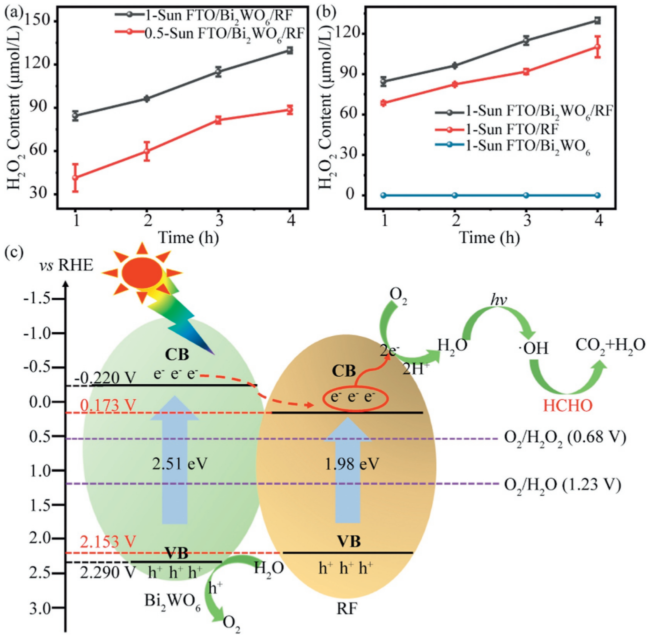

Fig. 4. Factors affecting photocatalytic H_2O_2 generation of FTO/Bi_2WO_6/RF. (a) H_2O_2 concentrations produced by FTO/Bi_2WO_6/RF under 1 sun and 0.5 sun of light irradiation. (b) H_2O_2 concentrations produced by FTO/Bi_2WO_6/RF, FTO/RF and FTO/Bi_2WO_6 under the same light intensity (1 sun). (c) Energy band diagram of Bi_2WO_6 and RF resin for different reactions.

The HCHO concentration was detected by national standard method (Fig. S7 in Supporting information). Then a schematic representation of HCHO degradation test is depicted in Fig. 5a. A closed cubic box ($6 \times 6 \times 6$ cm^3) was prepared with injection of HCHO gas containing FTO/Bi_2WO_6/RF film inside it. At intervals of every 15 min under sunlight conditions, gas samples were extracted from the box to measure the time-dependent HCHO concentration (Fig. S8 in Supporting information). The schematic diagram of the HCHO photocatalytic degradation and detection experiment is as shown in Fig. S9 (Supporting information). The concentration of HCHO in the box without FTO/Bi_2WO_6/RF film is around 0.18 mg/m^3, higher than the national standard for indoor HCHO concentration (0.08 mg/m^3). In contrast, for the box containing FTO/Bi_2WO_6/RF film, HCHO concentration is reduced to 0.03 mg/m^3 within 1 h, below the national standard. The degradation efficiency (η) was calculated using the following equation (Eq. 4):

$$\eta = \frac{C_t - C_0}{C} \times\ 100\% \tag{4}$$

where C_0 and C_t are the initial and after-reaction concentrations of HCHO. The degradation efficiency was as high as 84% (Fig. 5b), superior to other photocatalysts that have been reported under similar conditions. (Table S2 in Supporting information).

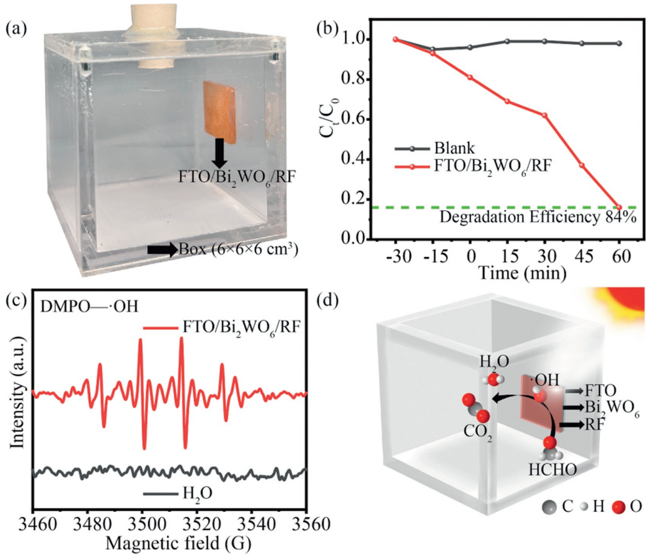

Fig. 5. (a) A closed box used to simulate the inhouse degradation experiment. (b) Efficiency of HCHO degradation within 1 h. (c) EPR of air in the box. (d) Schematic of indoor HCHO degradation mechanism.

These findings demonstrate the exceptional performance of the designed FTO/Bi$_2$WO$_6$/RF structure in indoor HCHO degradation in limited time-period. In this context, electron paramagnetic resonance (EPR) tests were conducted to investigate the active species responsible for formaldehyde degradation, as depicted in Fig. 5c. $^{\bullet}$OH played a crucial role. Furthermore, DFT calculations were performed to unravel the reaction kinetics (Table S3 in Supporting information) [49]. In the FTO/Bi$_2$WO$_6$/RF photocatalytic process, the total energy of the reactants (HCHO and *hv*) provided the initial energy at the outset of the reaction. The photoexcited $^{\bullet}$OH possessed a sufficiently high energy state to facilitate the degradation of formaldehyde molecules. The overall $\Delta G = -257.1$ kcal/mol for the entire reaction, indicating that the entire reaction is proceeding spontaneously towards the formation of more stable products like H_2O and CO_2. A negative ΔG value implies that the reaction is thermodynamically favorable, possessing sufficient driving force and requiring no additional energy input. Therefore, it is a thermodynamically favorable process for formaldehyde degradation.

Furthermore, the overall mechanism of HCHO degradation can be summarized in Fig. 5d. When sunlight irradiates on the surface of FTO/Bi$_2$WO$_6$/RF film, the light energy exceeds or equals the band gap energies of Bi$_2$WO$_6$ and RF, will promote electrons and holes separation within the photocatalyst. Heterojunction between Bi$_2$WO$_6$/RF facilitates transfer of photogenerated electrons from Bi$_2$WO$_6$ to RF. The photogenerated electrons in CB of RF are captured by O_2 for two-electron reduction being converting into H_2O_2. Subsequently, under light exposure, the H_2O_2 formed on FTO/Bi$_2$W$_6$/RF surface will be spitted into hydroxyl radicals capable of degrading formaldehyde into water and carbon dioxide [8,29].

In summary, a facile two-step hydrothermal method has been employed to successfully construct the FTO/Bi$_2$WO$_6$/RF heterojunction window. This novel and highly efficient photocatalyst can degrade up to 84% of indoor HCHO within 1 h, with a degradation rate of 0.15 mg m^{-3} h^{-1}. In this experiment, the national indoor formaldehyde standard (0.08 mg/m^3) was achieved within 1 h. The excellent photocatalytic performance is attributed to the Bi$_2$WO$_6$/RF heterojunction that promotes photogenerated electron transfer from Bi$_2$WO$_6$ to RF. This study presents innovative approach on integrating multilayer photocatalytic materials on substrate for effective removal of indoor HCHO, with potential applicability in degrading other VOCs.

Declaration of competing interest

The authors declare that they have no known competing financial interests or personal relationships that could have appeared to influence the work reported in this paper.

Acknowledgments

This work was financially supported by the National Key Research and Development Programme of China (No. 2021YFA1202500, H.C.), Foundation of Shenzhen Science, Technology and Innovation Commission (SSTIC) (Nos. 20231122110855002, JCYJ20200109141625078, H.C.), National Natural Science Foundation of China (No. 12174246, J.L.), Shenzhen Key Laboratory of Interfacial Science and Engineering of Materials (No. ZDSYS20200421111401738, H.C.), Natural Science Funds for Distinguished Young Scholar of Guangdong Province, China (No. 2020B151502094, H.C.). We acknowledge the technical support from the SUSTech Core Research Facilities at Southern University of Science and Technology.

Supplementary materials

Supplementary material associated with this article can be found, in the online version, at doi:10.1016/j.cclet.2023.109429.

References

[1] H. Ren, H. Weng, J. Huang, X. Lu, S.W. Joo, J. Alloys Compds. 919 (2022) 165843.
[2] R. Tong, L. Zhang, X. Yang, et al., J. Clean. Prod. 208 (2019) 1096–1108.
[3] S. Xia, G. Zhang, Y. Meng, et al., Appl. Catal. B: Environ. 278 (2020) 119266.
[4] W. Wang, H. Yu, K. Li, et al., J. Hazard. Mater. 415 (2021) 125649.
[5] V.J. Cogliano, Y. Grosse, R.A. Baan, et al., Environ. Health. Perspect. 113 (2005) 1205–1208.
[6] X. Yuan, X. Deng, C. Cai, et al., Green Energy Environ. 6 (2021) 759–770.
[7] H. Zhang, Z. Zheng, T. Yu, et al., Environ. Res. 205 (2022) 112550.
[8] L. Zhang, Q. Bao, B. Zhang, et al., JACS Au 2 (2022) 1651–1660.
[9] T. Cai, P. Zhang, X. Shen, et al., ACS Appl. Mater. Interfaces 12 (2020) 37147–37154.
[10] Y. Feng, L. Ling, J. Nie, et al., ACS Nano 11 (2017) 12411–12418.
[11] H. Belhadj, S. Hamid, P.K.J. Robertson, D.W. Bahnemann, ACS Catal. 7 (2017) 4753–4758.
[12] D. Mateo, J.L. Cerrillo, S. Durini, J. Gascon, Chem. Soc. Rev. 50 (2021) 2173–2210.
[13] P. Chen, F. Dong, M. Ran, J. Li, Chin. J. Catal. 39 (2018) 619–629.
[14] G. Liu, Y. Tian, B. Zhang, L. Wang, X. Zhang, J. Hazard. Mater. 367 (2019) 568–576.
[15] H. Nigar, I. Julian, R. Mallada, J. Santamaria, Environ. Sci. Technol. 52 (2018) 5892–5901.
[16] J. Mikulova, J. Barbierjr, S. Rossignol, et al., J. Catal. 251 (2007) 172–181.
[17] A. Wang, Q. Zhu, Z. Xing, Chem. Eng. J. 393 (2020) 124781.
[18] Q. Xu, L. Zhang, J. Yu, et al., Mater. Today. 21 (2018) 1042–1063.
[19] S. Sun, W. Wang, L. Zhang, J. Phys. Chem. C 116 (2012) 19413–19418.
[20] A. Kudo, I. Tsuji, H. Kato, Chem. Commun. 17 (2002) 1958–1959.
[21] Y. Shiraishi, T. Takii, T. Hagi, et al., Nat. Mater. 18 (2019) 985–993.
[22] L. Wang, B. Cheng, L. Zhang, J. Yu, Small 17 (2021) e2103447.
[23] Y. Wang, H. Huang, Z. Zhang, et al., Appl. Catal. B: Environ. 282 (2021) 119570.
[24] W. Wang, X. Li, F. Deng, et al., Chin. Chem. Lett. 33 (2022) 5200–5207.
[25] X. Xiong, J. Zhang, C. Chen, Ceram. Int. 48 (2022) 31970–31983.
[26] C. Zhang, G. Chen, C. Lv, ACS Sustain. Chem. Eng. 6 (2018) 11190–11195.
[27] P. Teng, Z. Li, S. Gao, et al., Opt. Mater. 121 (2021) 111508.
[28] M. Su, H. Sun, Z. Tian, Z. Zhao, P. Li, Appl. Catal. A: General 631 (2022) 118485.
[29] J. Wang, X. Xu, Y. Shen, J. Environ. Chem. Eng. 10 (2022) 107436.
[30] M. Wang, H. Xiao, Y. Ru, et al., Environ. Res. 212 (2022) 113148.
[31] M.T.L. Lai, K.M. Lee, T.C.K. Yang, J. Alloy Compd. 953 (2023) 169834.
[32] I. Gordon, F.C. Krebs, X. Mathew, Sol. Energ. Mat. Sol. C 133 (2015) A1–A6.
[33] Y. Shiraishi, S. Kanazawa, Y. Kofuji, et al., Angew. Chem. Int. Ed. 53 (2014) 13454–13459.
[34] Y. Kofuji, Y. Isobe, Y. Shiraishi, et al., J. Am. Chem. Soc. 138 (2016) 10019–10025.
[35] J. Wang, L. Yang, L. Zhang, et al., Chem. Eng. J. 420 (2021) 127639.
[36] Y. Hong, Y. Cho, E.M. Go, et al., Chem. Eng. J. 418 (2021) 129346.
[37] W. Fang, L. Wang, X. Meng, C. Li, J. Alloy Compd. 947 (2023) 169606.
[38] Z. Jiang, L. Wang, J. Lei, Y. Liu, J. Zhang, Appl. Catal. B: Environ. 241 (2019) 367–374.
[39] X. Qu, S. Hu, P. Li, et al., Diam. Relat. Mater. 86 (2018) 159–166.
[40] C. Li, G. Chen, J. Sun, et al., ACS Appl. Mater. Interfaces 7 (2015) 25716–25724.
[41] Y. Zhou, Y. Zhang, M. Lin, et al., Nat. Commun. 6 (2015) 8340.
[42] J. Sheng, X. Li, Y. Xu, ACS Catal. 4 (2014) 732–737.

[43] Y. Peng, Z. Bian, F. Wang, et al., J. Hazard. Mater. 462 (2023) 132797.
[44] K. Jinguji, M. Watanabe, R. Morita, et al., Catal.Today 426 (2024) 114400.
[45] T. Kakiuchi, S. Domae, T. Miyadi, et al., Electrochem. Commun. 126 (2021) 107021.
[46] G.A. Ferrero, K. Preuss, A. Marinovic, et al., ACS Nano 10 (2016) 5922–5932.
[47] X. Li, J. Yu, J. Low, et al., J. Mater. Chem. A 3 (2015) 2485–2534.
[48] Y. Chen, J. Fang, S. Lu, W. Xu, et al., J. Chem. Technolo. Biotechnol. 90 (2015) 947–954.
[49] N.K. Gour, K. Borthakur, S. Paul, R. Chandra Deka, Chemosphere 238 (2020) 124556.